Photochemistry and Photobiology, 20**, **: *–*

Special Issue Research Article

On the Development of a Light Dosimetry Planning Tool for Photodynamic Therapy in Arbitrary Shaped Cavities: Initial Results†

Thérèse E. M. van Doeveren[1,2], Rens Bouwmans[1], Nienke P. M. Wassenaar[1], Willem H. Schreuder[1], Maarten J. A. van Alphen[1], Ferdinand van der Heijden[3], I. Bing Tan[1,4,5], M. Barıs Karakullukçu[1] and Robert L. P. van Veen*[1]

[1]Verwelius 3D lab, Department of Head and Neck Surgery, The Netherlands Cancer Institute, Antoni van Leeuwenhoek Hospital, Amsterdam, The Netherlands
[2]Department Otolaryngology and Head and Neck Surgery, Erasmus University Medical Center, Rotterdam, The Netherlands
[3]Robotics and Mechatronics, Technical Medical Centre, University of Twente, Enschede, Netherlands
[4]Department of Otorhinolaryngology, Head and Neck Surgery, Maastricht University Medical Center, Maastricht, The Netherlands
[5]Department of Otorhinolaryngology, Faculty of Medicine, Dr. Sardjito General Hospital, Gadjah Mada University, Yogyakarta, Indonesia

Received 29 June 2019, revised 13 November 2019, accepted 27 December 2019, DOI: 10.1111/php.13216

ABSTRACT

Previous dosimetric studies during photodynamic therapy (PDT) of superficial lesions within a cavity such as the nasopharynx, demonstrated significant intra- and interpatient variations in fluence rate build-up as a result of tissue surface re-emitted and reflected photons, which depends on the optical properties. This scattering effect affects the response to PDT. Recently, a meta-tetra(hydroxyphenyl)chlorin-mediated PDT study of malignancies in the paranasal sinuses after salvage surgery was initiated. These geometries are complex in shape, with spatially varying optical properties. Therefore, preplanning and *in vivo* dosimetry is required to ensure an effective fluence delivered to the tumor. For this purpose, two 3D light distribution models were developed: first, a simple empirical model that directly calculates the fluence rate at the cavity surface using a simple linear function that includes the scatter contribution as function of the light source to surface distance. And second, an analytical model based on Lambert's cosine law assuming a global diffuse reflectance constant. The models were evaluated by means of three 3D printed optical phantoms and one porcine tissue phantom. Predictive fluence rate distributions of both models are within ± 20% accurate and have the potential to determine the optimal source location and light source output power settings.

INTRODUCTION

The clinical response to meta-tetra(hydroxyphenyl)chlorin (m-THPC, Foscan®)-mediated photodynamic therapy (PDT) of head and neck malignancies depends partially on the fluence rate and fluence, that is, light dose delivered to the target and risk areas. Studies have demonstrated that an excessive or conversely insufficient fluence rate will both result in a reduced cell response and insufficient degradation of the tumor (1–5). An excessive fluence rate will cause depletion of the photosensitizer and/or the oxygen in the tissue (4,6,7). Insufficient fluence rate will negatively affect the phototoxic reactions within the cell (1–3,6,7). High fluence rates may cause adverse reactions such as extensive edema, severe mucositis, increased pain perception, unintended necrosis and hyperthermia (1–3,5,8–10). A low fluence rate requires an extended illumination time to achieve an effective light dose (1–10). It is widely accepted that an empirically determined light dose of 20 $J \cdot cm^{-2}$ at a fluence rate of 100 $mW \cdot cm^{-2}$ (λ = 652nm) to the target area results in an optimal response to m-THPC (dose 0.15 mg kg^{-1} body weight)–mediated PDT of the head and neck area (11–18).

For easily accessible superficial lesions in the head and neck region, such as the floor of mouth, dosimetry is relatively straightforward. In these cases, for a given target area radius, assuming the spot is aimed onto the surface at a perpendicular angle, the distance of the microlens tip to the target area, along with the total source output power (W) can be calculated in order to deliver a homogeneous spot of 100 $mW \cdot cm^{-2}$ for 200 s. The organs at risk are shielded with red light absorbing cloth or black wax during the illumination. For less accessible superficial lesions such as oropharyngeal walls or base of tongue, a cylindrical balloon with a linear diffuser in its center is often employed (17,19). The length of the linear diffuser corresponds to the length of the lesion and its output power is set to generate an incident fluence rate of 100 $mW \cdot cm^{-2}$ at the surface of the balloon. For lesions in the nasopharynx, a dedicated light delivery applicator was developed to shield the soft palate and nasal cavity while allowing full efficient light coverage of the nasopharyngeal cavity (20).

Recently, we have reported m-THPC–mediated PDT in recurrent or residual malignant tumors of the sinonasal cavity (21).

*Corresponding author email: r.v.veen@nki.nl (Robert L. P. van Veen)
†This article is part of a Special Issue dedicated to Dr. Jarod Finlay.

These tumors can persist or recur despite treatment with surgery and/or (chemo) radiation. The vicinity of essential structures, combined with treatment-associated high morbidity risks, limits alternative treatment options, such as salvage surgery and/or reirradiation. Chemotherapy in these patients is not curative. Intracavity PDT demonstrated to be a feasible adjuvant therapy after surgical debulking to achieve local tumor control without the severe adverse effects associated with aforementioned conventional treatment options (21,22). However, achieving a reproducible and controlled dosimetric approach remained cumbersome. In the pilot study of Caesar et al., the light delivery was based on the total output power of the light source, using either a microlens, a linear diffuser, or a spherical bulb diffuser at certain distance to the target area, aiming a direct incident light term of 100 $mW{\cdot}cm^{-2}$ (21). The optimal source location was estimated preoperatively using 2D computed tomography (CT) and magnetic resonance (MR) images. The source was manually positioned and manually kept at this location, verified under endoscopic guidance. The fluence rate at the target area was monitored using multiple isotropic detectors connected to a dosimetry device (21–23). The laser was then activated and the illumination lasted until a cumulative light dose of 20 $J{\cdot}cm^{-2}$ was measured. Analysis of *in vivo* fluence rate measurements during sinonasal PDT showed substantial spatial and temporal variations within and between patients (T.E.M. van Doeveren et al., unpublished data). These variations may have a profound impact on the clinical response and clearly demonstrate the necessity for a standardized and reproducible dosimetric approach. The current approach lacks accurate positioning of the source, reproducibility and 3D light dosimetry planning.

Dosimetry planning and *in vivo* fluence rate measurements for intracavity PDT are necessary because of the integrating sphere effect that occurs when optically irradiating the inner surface of a hollow tissue geometry, like the bladder (24). Photons that are emitted from the source enter the tissue at the boundary after which they are subjected to absorption and scattering events. A portion of these photons will be backscattered into the cavity and re-enter the tissue at a different location inside the cavity, resulting in a fluence rate build-up. The fluence rate at the tissue surface will be higher than the nonscattered light, that is, direct incident term emanating from the source. The amount of light that is backscattered depends on the tissue optical properties such as the scatter function, absorption and scattering coefficient. This build-up in fluence rate will influence the amount and rate of the photosensitizer activation and thus has the potential to alter the clinical response. This integrating sphere effect has been observed in several dosimetric PDT studies (3,10,17,20,24–32). For example, van Veen et al. demonstrated a fluence rate build-up of up to 4.5 times higher than the nonscattered direct incident light term from the source during m-THPC–mediated PDT of the nasopharynx (30). Quon et al. observed a build-up factor of 5 times during transoral robotic surgery (TORS)-guided PDT of the oropharynx (17).

Hollow cavities such as the esophagus or trachea can be described as cylinders, or in case of the bladder as an ellipsoidal shape, which allows a straightforward dosimetric fluence rate distribution planning approach, based on surface area and total output power (10,24,26). However, the hollow defect that remains after salvage surgery of the sinonasal cavity is complex in geometry and varies in volume and surface area between patients. These geometries cannot be simply approximated by a well-defined shape such as a hollow cylinder or sphere but require a more dedicated approach. In addition, the optical properties vary within the geometry and between patients (33–37).

The primary aim of this study is to develop light dosimetry models, allowing reliable calculations of the fluence rate at the surface of these complex sinonasal cavities while taking tissue backscattering into account. The goal is to develop two simple, fast and easily applicable dosimetry tools that merely require a 3D reconstructed model from CT image data and a series of pre-PDT patient optical measurements that enables calculation of the fluence rate including the scatter contribution.

For this purpose, three 3D printed optical phantoms of sinonasal cavities of patients who have undergone surgical resection of a sinonasal malignancy were constructed. The optical properties of the print material (Acrylonitrile Butadiene Styrene (ABS)) are approximately those of human mucosal tissue (20,38) with respect to the scattering coefficient. In addition, a clinically more relevant porcine tissue phantom was developed. Dosimetry experiments were conducted on these phantoms using a spherical diffuser and multiple isotropic detectors. Diffuse reflectance spectroscopy (DRS) was used to determine the phantom's optical properties. From these results, an empirical 3D light distribution model was established. Secondly, an analytical model was developed. The analytical model is based on diffuse Lambertian reflectance and is initially used to validate the reliability of the empirical model (39). Both models are based on the specific sinonasal geometry obtained from CT image data.

MATERIALS AND METHODS

Two 3D light distribution models were developed: an empirical model derived from the phantom's fluence rate data, and an analytical model based on the phantom's optical properties. The input variables of the empirical model are, first, the build-up factor function β (r), where r is the distance between the source and detector/cavity surface. Second, the total output power of the spherical bulb diffuser P_{out} (mW) and third, a high-resolution 3D patient-specific surfaces mesh, consisting of triangular faces and vertices (~10.000 faces, ~1.3 mm^2 per face). The input variables of the analytical model, which is based on Lambertian cosine law, are the medium's diffuse reflectance coefficient *Rd*, the same mesh surface as the empirical model and the total output power of the spherical bulb diffuser P_{out} (mW). Both models were developed in MATLAB™ (MATLAB, MathWorks Inc., MA). To evaluate both models, three 3D printed ABS optical phantoms and a separate porcine tissue phantom were constructed. The validity of both, the analytical model and the empirical model, was evaluated by comparing the actual fluence rate as measured in the ABS optical phantoms and the porcine tissue phantom, with the calculated fluence rate at eight different measurement locations. A flowchart of the research methodology is depicted in Fig. 1.

ABS optical phantoms. The fluence rate at the inner surface of a cavity depends on the geometry and optical properties. For this study, only the influence of the geometry is investigated. Three solid phantoms were printed in white ABS (Materialise, Leuven, Belgium). The optical properties, with respect to the reduced scattering coefficients, approximate that of tissue and were determined by three sequential spatially resolved DRS measurements on a solid bulky section of the phantom (40). In addition, DRS measurements were performed on a volunteer's oral buccal mucosa. An average reduced scattering coefficient (μ_s') at λ = 652 nm was determined to be 8.6 cm^{-1} for ABS white and 12.8 cm^{-1} for oral buccal mucosal tissue. An average absorption coefficient (μ_a) at λ = 652 nm was 0.01 cm^{-1} for ABS white and 0.12 cm^{-1} for oral buccal mucosal tissue. The possible consequences of the difference in optical properties are discussed later in the manuscript.

Postoperative CT data of three different representative patients: that is, eligible for sinonasal PDT, who had undergone sinonasal salvage surgery were selected. The geometry of the 3D ABS optical phantoms was obtained using Hounsfield threshold segmentation to separate air from

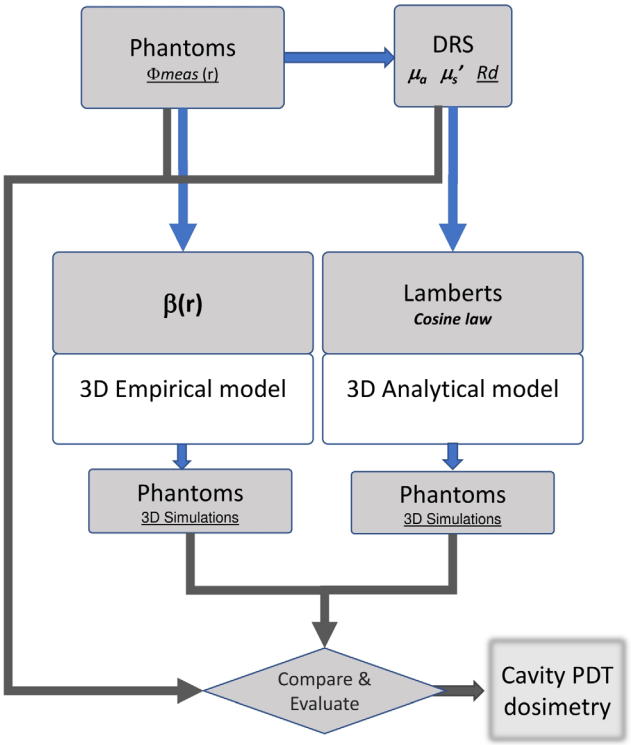

Figure 1. Flowchart of the conducted research. Three ABS optical phantoms and one porcine tissue phantom were constructed. DRS was used to determine *Rd* from the μ_a and μ_s' results. A series of multiple fluence measurements Φ_{meas} *(r)* were performed on all four phantoms. An empirical model was derived from the experimental fluence rate data, and an analytical model was developed. After which both developed models were used to simulate the 3D fluence rate distribution of all four phantoms. The simulation results were compared with the actual measurements. Both models were compared and evaluated.

tissue in 3D slicer (41). Tissue and bony structures were considered to be equal, which means that no layered structures were incorporated. The minimal distance between the inner surface of the sinonasal cavity and the exterior surface of the phantom was set to be 2 cm, thereby minimizing the possible contribution of backscattering from the exterior boundary into the cavity, as well as loss to the external space. The volume and the total cavity surface area were determined for all three ABS optical phantoms.

After printing the ABS optical phantoms, a total of eight 1-mm-outer diameter (OD) holes were drilled externally into the cavity, entering the cavity on various locations of interest. These holes facilitate the passage and positioning of the isotropic detectors (spherical tip OD 0.85 mm, model IP85; Medlight S.A., Ecublens, Switzerland) into the cavity. The phantoms were printed in two separate adjacent parts through the middle of the sagittal plane, to allow visual verification regarding the positioning of the eight isotropic detectors and the spherical bulb diffuser. Rendering of the ABS optical phantom is shown in Fig. 2.

The spherical tip of the isotropic detector was positioned directly above the surface of the cavity. For this study, only the spherical bulb diffuser (Medlight SA, Ecublens, Switzerland) was used as the PDT light source. The spherical bulb diffuser was connected to a 2 W diode laser (Ceralas PDT, Biolitec, Bonn, Germany) emitting at λ = 652 nm. The diffuser was positioned in the center of the cavity (slightly posterior) and pulled back ~10 mm (anterior) toward the nostril through a transparent Perspex tube. In total, 16 measurements per ABS optical phantom were made. The isotropic detectors measure the fluence rate by collecting the direct incident light (E_{inc}) from the source, as well as the diffuse scattered light from all incoming directions, that is, $\phi_{meas} = E_{inc} + (\phi_{sc} + \phi_{bsc})$.

A cone beam CT (CBCT) was made of the complete ABS optical phantom including the incorporated isotropic detectors and spherical

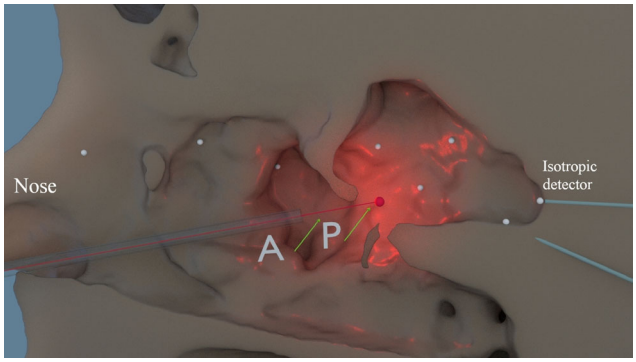

Figure 2. A rendering of the medial view of an ABS optical phantom based on a patient who underwent an ethmoidectomy and sphenoidectomy. The spherical bulb diffuser (in red) is placed at two different locations within the nasal cavity; the "*A*" anterior and "*P*" posterior position. The white dots show the spherical tip of the isotropic detectors inside the cavity.

bulb diffuser at position. CBCT imaging was done for two spherical bulb diffuser positions: an anterior (A) and a posterior (P) position. From the 3D reconstructed CBCT images, the exact distance between the center of the spherical bulb diffuser and the isotropic detectors was determined. This distance was used to calculate the local build-up factor β (r) at the position of the isotropic detector at the inner surface of the cavity.

$$\beta(r) = \frac{\phi_{\text{meas}}(r)}{\left[\frac{P_{\text{out}}}{4\pi r^2}\right]} \quad (1)$$

where r (cm) represents the distance between the light source, that is, the spherical bulb diffuser and the isotropic detector, P_{out} the total output power of the source (mW), ϕ_{meas} (mW·cm^{-2}) the measured fluence rate and the denominator term expresses the direct incident term E_{inc}. The β (r) function was derived in each individual ABS optical phantom, using all valid fluence rate measurements (*i.e.* the detectors that are exposed to E_{inc}, with the spherical bulb diffuser at two positions (A and P)). The output power of the spherical bulb diffuser was set at 500 mW. The empirical model will be derived from the dosimetry data for all ABS optical phantoms and are therefore considered to be a result.

Porcine tissue phantom. The *ex vivo* porcine tissue phantom was developed to mimic a more clinically relevant setting, that is, a higher μ_a as compared to the ABS optical phantom.

The porcine tissue phantom consists of a 3D printed shell, cloaked inside with an average ~15 mm thick homogeneous layer of porcine muscle tissue sutured and secured to the rigid mesh structure, thus creating a tissue cavity that mimics sinonasal geometry. The 3D Voronoi mesh structure was created in Autodesk® Meshmixer. First, a simplified slightly oversized sinonasal cavity shape was made. The shape was hollowed and meshed in order to form a shell-like structure as can be seen in Fig. 3.

Diffuse reflectance spectroscopy measurements were performed on the porcine tissue. An average reduced scattering coefficient (μ_s') at λ = 652 nm was determined to be 10.4 cm^{-1}, and the absorption coefficient (μ_a) was 0.13 cm^{-1}. The measured optical properties were similar to buccal mucosa (μ_s' = 12.8 cm^{-1} and μ_a = 0.12 cm^{-1}).

Infusion needles were used to guide the isotropic detectors to the inner surface of the tissue cavity. A fixed rigid transparent Perspex tube was used to guide and steadily position the spherical bulb diffuser to an anterior and posterior position inside the cavity. The difference between both source positions (sagittal plane) was approximately ~12 mm. The same CBCT approach as used for the ABS optical phantoms was employed to determine the exact distances between the center of the spherical diffuser and the isotropic detectors. For each location, the local build-up factor β was calculated. The output power of the spherical bulb diffuser was 1500 mW.

Empirical model. The empirical model aims to calculate the fluence (rate) at the surface of the cavity, that is, for all triangular faces using a single linear equation that directly calculates the fluence rate

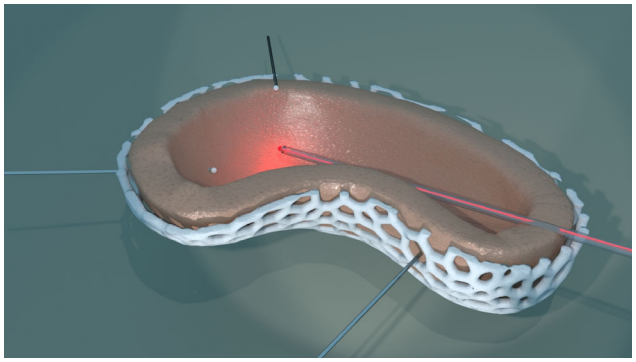

Figure 3. A rendering of half the porcine tissue phantom. Depicted is the 3D printed shell with a Voronoi mesh structure (white) including the porcine tissue layer secured to the inner shell by sutures. A transparent Perspex tube was used to guide and hold the spherical diffuser in position. Three isotropic detectors are shown as an example in this figure.

including the scatter terms. The model eventually should be able to calculate the fluence rate distribution at the surface for all possible source locations in order to find the optimal source location (OSL) at which the target area is effectively illuminated during PDT, while minimizing the light dose to the organs at risk. Computation speed is therefore important.

The local build-up factor β (Eq. 1) was determined for all measurement locations at the surface of the three ABS optical phantoms. The aim was to investigate systemic behavior of β (r) in the arbitrary shaped complex geometries. The cavity volume and surface area of the three ABS optical phantoms were determined via the 3D meshes to investigate their relation with β (r). Shadow areas or niches in the cavity, that is, faces that are not directly in the line of sight with the source, were excluded from the empirical model.

Analytical model. The developed analytical model assumes Lamberts cosine law, that is, the incident radiant intensity of light emanating from an ideal diffuse light emitting source and is directly proportional to the cosine of the angle θ between the direction of the incidence (from incident surface to emitting source) and the surface normal of the emitting source. The diffuse reflectance constant *Rd* determines the fraction of incident light that is Lambertian being re-emitted from the surface back into the cavity. The model first calculates the direct irradiance, that is, "direct incident fluence rate" term E_{inc} for each face. Secondly, each face re-emits a part of the light, which is not absorbed, back into the cavity, contributing to the fluence rate of other faces. Therefore, photons will travel from the light source to the first face, toward the second, toward the third, etc. until a certain amount of reflections, at which the total amount of light is below 1% to that emitted by the source. In summary, the fluence rate at the surface of a single face is comprised of a direct incident term E_{inc} (Eq. 2), a diffuse re-emitted term (ϕ_{bsc}) and a diffuse incident term (ϕ_{sc}). The total diffuse scattered term including the direct incident term (E_{inc}) gives the fluence rate at the surface ($\phi_{face,\ tot}$). $\phi_{face,\ tot} = E_{inc} + (\phi_{bsc} + \phi_{sc})$.

$$E_{inc} = \frac{P_{out}\mathrm{Cos}\ (\theta)}{4\pi\|\boldsymbol{\nu}_{so}\|^2} f_{inc} \tag{2}$$

where E_{inc} is the irradiance due to direct incident light from the light source, $\|\boldsymbol{\nu}_{so}\|$ the magnitude of vector $\boldsymbol{\nu}_{so}$, that is, the distance between the source and the center of the face, and f_{inc} the fraction of initial light reaching the face, for example, located at the shadow boundaries. f_{inc} is either 1, 2/3, 1/3 or 0, depending on the amount of vertices of the face that lay in direct line with the source. The total incident term onto a single surface mesh face ϕ_{face} is calculated according Eq. (3).

$$\phi_{face} = E_{inc} + \sum_{j=1}^{n}\sum_{k=1}^{m} \phi_{sc_{j,k}} \tag{3}$$

where n represents the number of reflections simulated and m is the total amount of faces in the mesh. Adding the total re-emitted diffuse component results in the fluence rate (Eq. 4).

$$\phi_{face,tot} = (1 + Rd)\phi_{face} \tag{4}$$

The diffuse reflectance coefficient *Rd* was calculated according to Eq. (5) (42).

$$Rd = \frac{a'}{2}\left[1 + e^{-\left(\frac{4}{3}\right)A\sqrt{3\cdot(1-a')}}\right] e^{-\sqrt{3\cdot(1-a')}} \tag{5}$$

where $a' = \mu_s'/(\mu_s' + \mu_a)$ is the transport albedo and $A = (1 + r_d)/(1 - r_d)$ represents the internal reflection parameter and where $r_d = -1.44\, n_{rel}^{-2} + 0.71\, n_{rel}^{-1} + 0.668 + 0.0636\, n_{rel}$ (43), $n_{ABS} = 1.52$, $n_{air} = 1$ and $n_{tissue} = 1.4$ and $n_{rel} = n_{medium}/n_{air}$ are the refractive indices. Using the obtained values for μ_a and μ_s' from the DRS measurements, that is, ABS optical phantom, *ex vivo* porcine tissue and *in vivo* human mucosal tissue resulted in $Rd_{ABS} = 0.81$, $Rd_{por} = 0.58$ and $Rd_{tissue} = 0.62$. To cross-validate the reliability of the DRS measurement results, Rd_{medium} was set as fit parameter in the range of $Rd_{medium} \pm 0.1$ (0.01 interval). The simulations were run on a regular Intel® Core™ i5-8250U CPU (8GB).

RESULTS

In the following paragraphs, the results for each specific phantom and model are presented, including a comparison between both developed models.

ABS optical phantoms

Empirical model. The results of the fluence rate ϕ_{meas} ($mW{\cdot}cm^{-2}$) measurements at the cavity surface for three different ABS optical phantoms, at eight different isotropic detector locations and two light source positions are shown in Table 1.

The output power of the spherical bulb diffuser was 500 mW. The distances between the light source and isotropic detectors ranged from 0.6 up to 5.7 cm. All measurements located in regions that were not directly illuminated by the spherical diffuser, that is, shadow areas, were excluded from the build-up factor β (r) analysis, since direct incident fluence rate term is required. Note that shadow areas do however receive scatter contribution from its complete surrounding area. The isotropic detectors in shadow areas were digitally identified by analyzing the 3D reconstructed CBCT data. These detectors only received a scatter contribution as shown in Table 1. By repositioning the spherical bulb diffuser from the posterior position (P) to the anterior position (A), the isotropic detector could be directly illuminated in position A although not in P and vice versa.

The build-up factor was calculated according to Eq. (1) for all valid fluence rate measurements, that is, directly illuminated by the light source and for each phantom. The data suggest a linear relation according to Eq. (6) between the source-detector distances and was therefore fit through the data points. It is assumed that the build-up factor cannot be lower than 1 for source-detector distances approaching 0.

$$\beta(r) = ar + 1 \tag{6}$$

where r is the distance between the spherical bulb diffuser and the inner surface of the cavity. The slope is represented by a. The linear function β (r) was fit through all available measurement points, that is, $n = 6$, $n = 8$ and $n = 12$ for phantoms 1, 2 and 3, respectively. The slope a values were 6.0, 4.6 and 5.1 for phantom 1, 2 and 3, respectively. Figure 4 shows the results of all three phantoms combined.

Consequently, fitting β (r) through less data points would result in a different value for a. To investigate the influence of

Table 1. Fluence rate measurements using isotropic detectors at eight different locations within the ABS optical phantoms.

Phantom number	Position	P_{out} (mW)	Detector 1 (mW·cm^{-2})	Detector 2 (mW·cm^{-2})	Detector 3 (mW·cm^{-2})	Detector 4 (mW·cm^{-2})	Detector 5 (mW·cm^{-2})	Detector 6 (mW·cm^{-2})	Detector 7 (mW·cm^{-2})	Detector 8 (mW·cm^{-2})
1	A	500	85.5	30.1*	50.6	42.4*	183.4	21.7*	75.8*	70.4
1	P	500	80.0	38.1	71.4*	56.8*	115.8	18.6*	77.7*	68.4
2	A	500	209.6	118.8	156.2*	137.7*	223.4	242.6*	150.8	131.8*
2	P	500	243.1*	163.9*	183.1*	187.7*	239.1*	360.7	215.1*	185.7
3	A	500	97.6	121.9	88.4*	95.3	73.2*	54.7	60.3	15.6*
3	P	500	100.8	132.4	97.6	90.8	92.5	55.0	61.1	16.5*

The measurements have a systematic error (after calibration) of 5-10%. In the column "*Position*", "*A*" stands for an anterior position and "*P*" for a posterior position of the spherical bulb diffuser. The isotropic detectors that were not directly exposed to the light emanating from the source are marked with an asterisk (*).

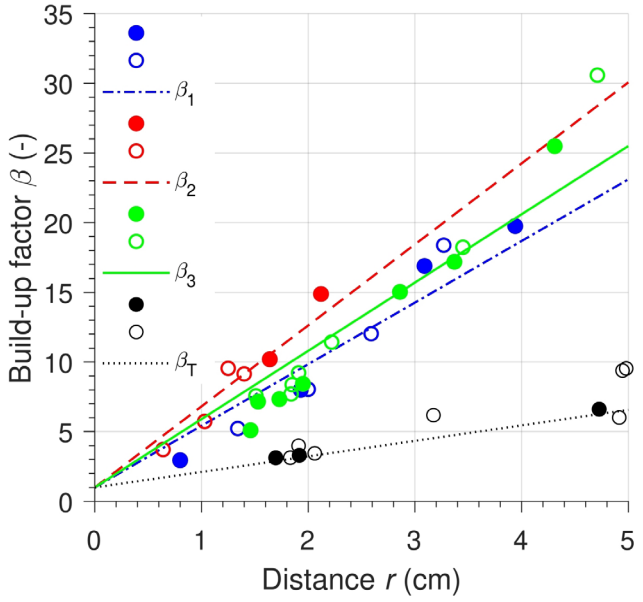

Figure 4. The build-up factor β (r) as a function of the source-detector distance (r) for the three ABS optical phantoms (colored) and the porcine phantom (black) using a spherical bulb diffuser. The visualized points in the graph represent the build-up factor for each individual isotropic detector receiving direct incident light from the spherical bulb diffuser at different distances from the light source. The isotropic detectors that were not directly illuminated by the spherical bulb diffuser, that is, the "shadow areas" were excluded from the build-up factor β (r) analysis. The measurements were performed at two different light source positions; the "anterior" position indicated by the solid dots ● and the "posterior" position in circles ○. The R^2 values of the ABS optical phantoms were 0.91, 0.92 and 0.89 for phantoms 1, 2 and 3, respectively. The slope a of the porcine phantom showed a value of 1.3 and R^2 of the fit was 0.81.

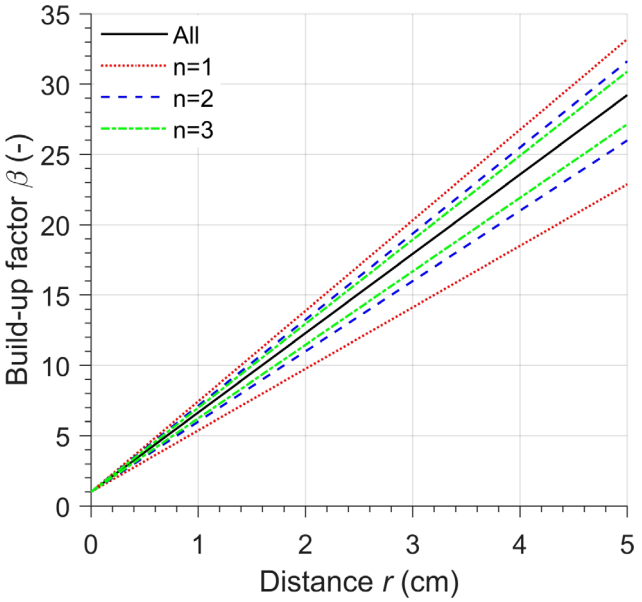

Figure 5. Demonstrates the variance in build-up factor as a result of the number of measuring probes used to determine β (r) for phantom 2. "*All*" is the build-up function determined with all available valid fluence rate measuring points; "*n*" indicates the number of measuring probes used to determine the build-up function. These lines indicate the absolute maximal and minimal values of the slope a of β (r) per n used measuring probes.

the number of measurements n on the variance of the slope a, β (r) was fit again using fewer data points. This was calculated for n = 1, n = 2 and n = 3 for each phantom, for example, for the eight available valid data points of ABS optical phantom 1 (Table 1, Fig. 5). A β (r) was fit through each unique combination of n separately, therefore resulting in maximum and minimum slope a values. For example, when n = 2 for phantom 1, all combinations of two measurements points (locations) out of the available eight were used to fit the slope a, and therefore resulting in the variance of slope a. Figure 5 shows the variance of β (r) for n = 1, n = 2, n = 3 and all (n = 6) available valid fluence rate measurements for phantom 1. Phantoms 1 and 3 demonstrated comparable results. The standard deviations (SD) for the slope a for n = 1, 2 and 3 were 1.03, 0.56 and 0.37, respectively. Phantom 2 and 3 showed similar results.

The more fluence rate measurements n at various distances from the source, the more accurate the predicted values of the empirical model will become. The fluence rate distribution over the entire surface was calculated using the predetermined phantom-specific β (r) function. The 3D simulated fluence rates that corresponded to the location, that is, face of the isotropic detectors are plotted against the actual measured fluence rate in Fig. 6 for all three ABS optical phantoms.

The slope a of the three β (r) functions was plotted as a function of the ratio between the cavities total surface areas and volumes of the three surface meshes and are shown in Fig. 7. A high surface to volume ratio is associated with increasing surface irregularities, that is, more bulges and niches, and results in a higher slope a value.

Analytical model. The fluence rate at the surface of ABS optical phantom 1, 2 and 3 was calculated. The total source

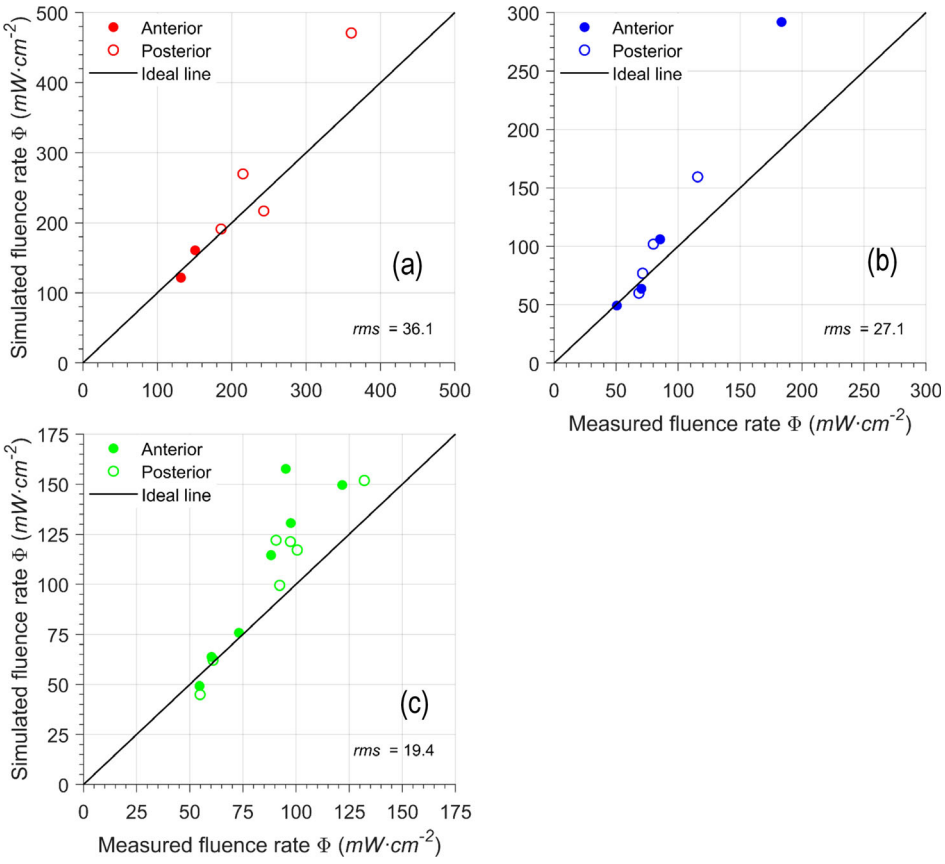

Figure 6. The 3D empirically simulated fluence rates for all three ABS phantoms (a-c) at the mesh faces that correspond with the location of the actual isotropic detectors plotted against the measured fluence rate. The fluence rate distribution over the entire mesh surface was calculated using the predetermined phantom-specific β (r) function. The performance of each simulation is expressed in a root mean square (rms) value. The ideal line represents $\phi_{meas} = \phi_{sim}$.

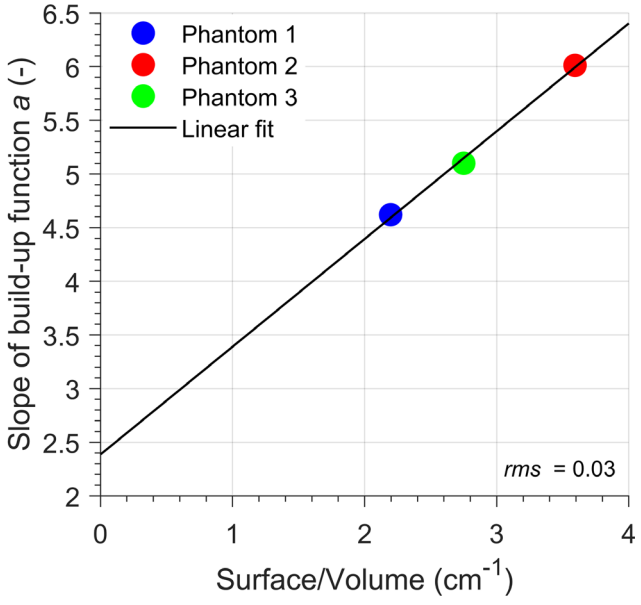

Figure 7. The slope a of β (r) of the three ABS optical phantoms plotted as a function of the ratio between the surface areas and volumes of the three ABS optical phantoms.

output power served as input parameter for the model (P_{out} = 500mW) and corresponded to the P_{out} used in the fluence rate experiments and the ABS optical phantoms. The diffuse reflection coefficient Rd for ABS white was first calculated according to Eq. (5) using the obtained results for μ_s' and μ_a from the DRS measurements and resulted in an Rd_{ABS} value of 0.81. These DRS measurements are associated with some degree of uncertainty (40,44). Rd was therefore set as a fit parameter to match the fluence rate as measured by all isotropic detectors (*i.e.* including those in the shadow areas) to those calculated. The faces that are not in the direct line of sight of the spherical bulb diffuser do however receive a fraction of the total re-emitted backscattered light. The model determines the fluence rate for these shadow areas as opposed to the empirical model. Rd was fit in steps of 0.01 in the range of $Rd_{ABS} \pm 0.1$, that is, 0.7–0.9 in order to minimize the root mean square (rms) between the measured fluence rate and the predicted fluence rate by the analytical model. An Rd_{ABS} of 0.81 generated the best fit, with an average rms of 20.8 for all three phantoms, and was in agreement with the Rd_{ABS} as calculated according to Eq. (5). After 22 sequential reflections ($P_{out}0.81^{22} = P_{out}0.0097$), the available amount of energy was less than 1% of the initial amount. This value indicates the end of the fit. Figure 8 shows the

results for all three ABS optical phantoms including a plot of the fits rms as function of the Rd_{ABS}. In phantom 1, there are two points that have a simulated fluence rate of zero while the measured fluence rate is around 30–40 mW·cm^{-2}. These two points are located in a secluded sinonasal cavity that was not directly connected to the main target location. Note that the number of valid measurements is higher compared with the empirical model. The analytical model is capable of calculating the fluence rate at faces who are not receiving direct light by the light source.

Porcine tissue phantom

The results of the eight fluence rate measurements at the inner tissue surface of the porcine tissue phantom are shown in Table 2.

The light source to isotropic detector distances were calculated from the 3D reconstructed CBCT image data, in conjunction with the localization of the faces that corresponded to the actual isotropic detector positions. The distances ranged from 1.7 up to 7.2 cm.

Empirical model. First, the β (r) function was determined from the experimental data, as shown in Fig. 4. The variances were smaller compared with those calculated for the ABS optical phantoms. Based on the phantom's specific β (r), the fluence rate distribution over the mesh surface was calculated. The simulated fluence rate versus the measured fluence rate is shown in Fig. 9.

Analytical model. The *Rd* according to Eq. (5) of the porcine tissue was 0.58. *Rd* was therefore fit around this value ($Rd_{por} \pm 0.1$. range 0.5–0.7) by minimizing the rms of the measured and simulated fluence rate values. An *Rd* of 0.62 was obtained from the fit. The simulated fluence rate versus the measured fluence rate is shown in Fig. 9. The amount of reflections simulated was set to 10 ($P_{out}0.62^{10} = 0.0084$).

Model comparison

A summary of the comparison between several clinically relevant specifications of the empirical and analytical model are shown in Table 3.

An example of a 3D fluence rate plot and histogram of ABS optical phantom 2 is depicted in Fig. 10 (right), an additional histogram depicting the absolute difference (Δ) between the calculated fluence rate per face of both models, for example, empirical versus analytical, is shown on the far right. Large differences originate from faces with a high fluence rate. The shadow areas were not compared. The calculation time to determine the 3D fluence rate distribution for the analytical model is fairly slow, for example, ~8 s for a given source location as compared to 8.0 × 10^{-5} s for the empirical model.

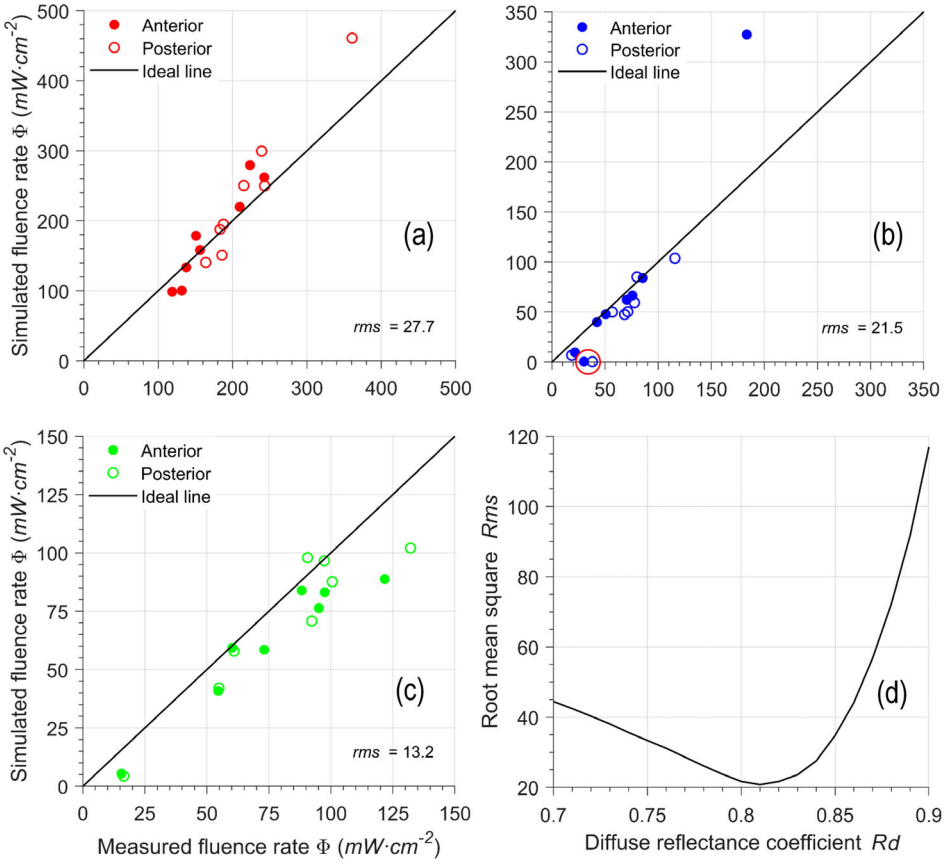

Figure 8. The result of the analytical model for all three ABS optical phantoms (a–c). Plot (d) depicts the root mean square (rms) as a function of the fit parameter *Rd*. Note that in plot (b), ABS optical phantom 2, there are two points that have a simulated fluence rate of zero while the measured fluence rate is around 30–40 mW·cm^{-2}. These two points are encircled with a red line and are located in a sinonasal cavity that is not directly connected to the main target cavity.

Table 2. Fluence rate measurements using a spherical bulb diffuser light source at the inner surface of the porcine tissue phantom.

Position	Source output (mW)	Detector 1 (mW·cm^{-2})	Detector 2 (mW·cm^{-2})	Detector 3 (mW·cm^{-2})	Detector 4 (mW·cm^{-2})	Detector 5 (mW·cm^{-2})	Detector 6 (mW·cm^{-2})	Detector 7 (mW·cm^{-2})	Detector 8 (mW·cm^{-2})
A	1500	129.7	35.3	28.1	20.3	12.7	4.7	7.5	107.2
P	1500	96.8	11.4	73.3	45.9	45.8	15.8	29.7	130.5

In column "*Position*," "*A*" stands for an anterior position and "*P*" for a posterior position of the light source.

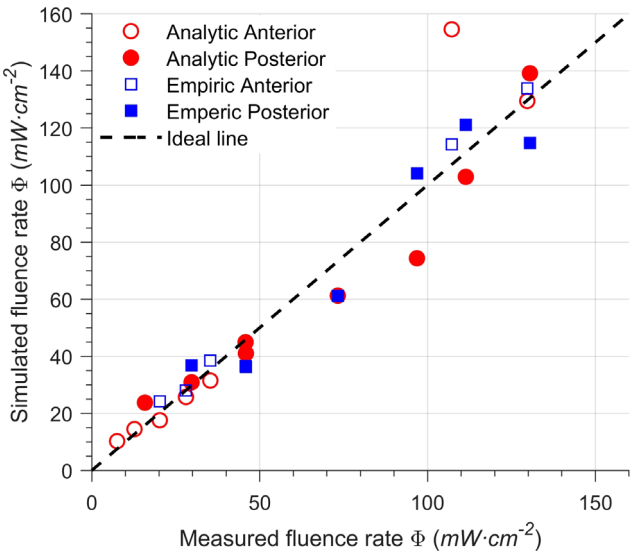

Figure 9. Based on the porcine tissue phantom-specific β (r), the fluence rate distribution over the entire mesh surface was calculated with the empirical and analytical models. This plot shows the simulated fluence rate *versus* the measured fluence rate at the actual location of the isotropic detector.

Table 3. A comparison between both developed models.

Subject	Empiric model	Analytic model
Calculation speed (*ABS optical phantom*—porcine tissue phantom)	Fast (8.0×10^{-5}–8.0×10^{-5} s)	Slow (15.9–7.9 s)
Rms (*ABS optical phantom*—porcine tissue phantom)	27.5–7.4	20.8–8.2
Variables	β (r)	*Rd*
Requirements to perform calculations	Fluence rate(s) measurements at known source detectors distance. CT imaging.	A measurement of μ_a, μ_s' or *Rd* direct. CT imaging.
Shadow determination	Estimated	Feasible
Pitfalls	Linear assumption of β (r) through (0,1).	Simplistic ray tracing algorithm and inverse square law usage for large faces relative to the distance between source and face.
Clinical applicability	Easier to implement	Harder to implement

DISCUSSION

The primary aim of this study was to investigate the fluence rate distribution in a complex arbitrarily shaped sinonasal cavity and to gain insight regarding the underlying mechanisms. The results presented are the initial results. The focus of this study was solely on the development of fluence rate distribution models for PDT in complex hollow geometries. The clinical response to PDT is far more complex and includes among other things, influences of tissue oxygenation, vasculature, photosensitizer concentration and the amount of reactive oxygen species. These variables were not taken into consideration.

From the fluence rate data, an empirical model was derived. In addition, a relatively simple analytical model was developed to cross-validate with the empirical model using the DRS and fluence rate results from the ABS optical phantoms as well as the more clinically realistic porcine tissue phantom.

The fluence rate in the sinonasal cavity is determined by the geometry and optical properties. Depending on the location of the tumor, the original sinonasal geometry is altered by the salvage surgery, varying from a (combination of) medial maxillectomy, ethmoidectomy or sphenoidectomy. In addition, there is an expected variation in optical properties within every sinonasal cavity (33–37). A variety of tissue types are to be expected in the sinonasal cavity after salvage surgery, such as exposed bone, varying thickness of mucosa, scar tissue, mucus and crusts. Each of them having different optical properties. A predictive accurate analytical model, that is, Finite Element Method or Numerical model (Monte Carlo Simulation) would therefore require accurate and high spatial resolution knowledge of the local *in vivo* absorption coefficient, the scattering coefficient and the scatter function, for example, the Henyey-Greenstein phase function. In addition, these accurate analytical and numerical models are complex and associated with long computation times.

The tissue optical parameters vary across the surface and in depth. These parameters are difficult to measure *in vivo*, requiring DRS devices and multiple *in vivo* measurements, and are therefore considered clinically impractical. However, these measurements may deem to be necessary prior to PDT in order to calculate the fluence rate distribution. The simpler faster models as presented, provide the surgeon with 3D information regarding the light dose and fluence rate distribution with an accuracy of $\pm$ 25% and is considered clinically beneficial and acceptable.

The empirical model

The ABS optical phantoms, derived from actual patient CT images accurately, mimic the geometry of sinonasal cavities. The ABS optical properties however are homogeneously distributed compared with an *in vivo* setting and equal for the three ABS optical phantoms. The fluence rate distribution therefore only depends on the geometry (volume, surface area and curvature/shape) of the phantom. The larger the surface to volume ratio, the larger slope a becomes. If the cavity surface becomes more irregular, meaning the surface area increases as compared to the volume, due to increasing number of bulges and niches that

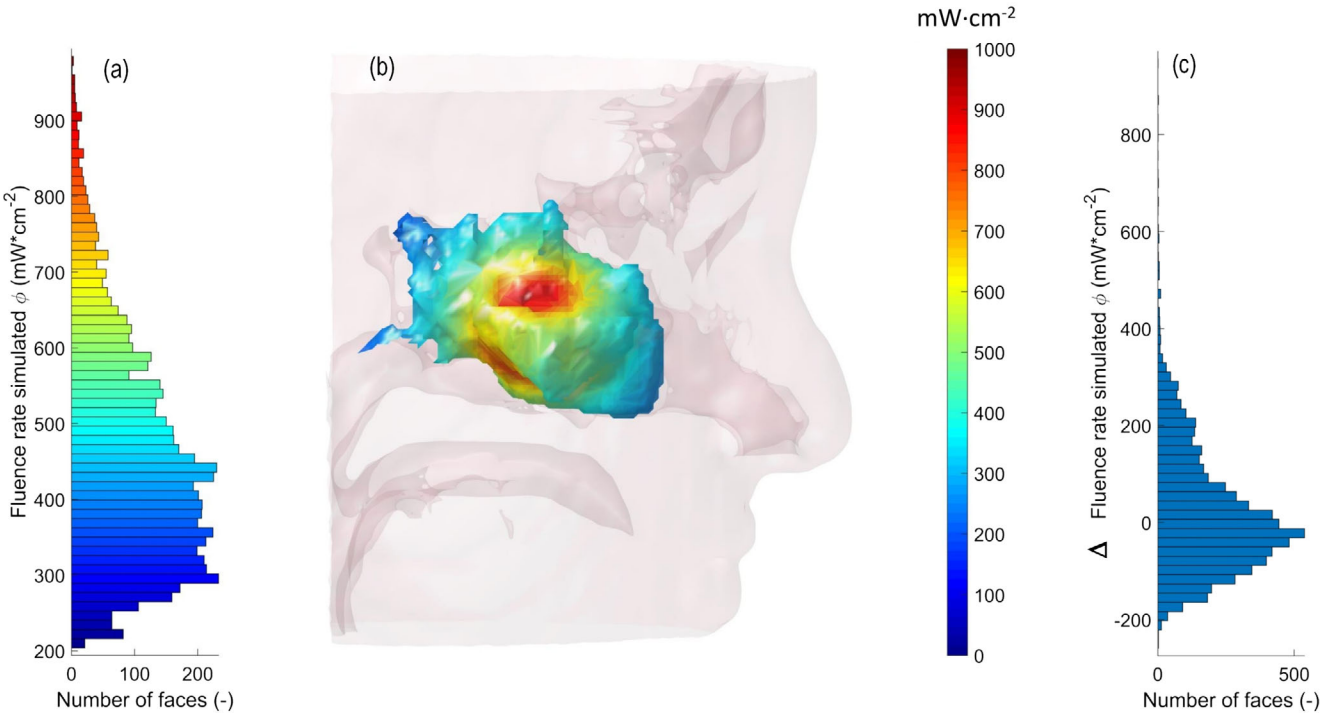

Figure 10. An example of a 3D mesh fluence rate plot of the ABS optical phantom 2 generated by the empirical model (sagittal view). On the left, the corresponding fluence rate distribution-face histogram. The source output power was set at 1500 mW. The source position was the same for both models. On the right, the false-color scale of the fluence rate ranging from 0 (blue) op to 1000 mW·cm^{-2} (red). The histogram on the right shows the absolute difference per face between both models.

result from surgery, the slope will increase as shown in Fig. 7. This observation implies that slope *a* could potentially be derived from CT data, provided that the global optical properties are known and comparable between patients. In order to demonstrate this concept, additional *in vivo* fluence rate data with known source-detector distances are required.

The reduced scattering coefficient of the ABS material was determined by DRS measurements and comparable to that of *in vivo* mucosal tissue (8.6 cm^{-1} *vs* 12.8 cm^{-1}) and porcine tissue (8.6 cm^{-1} *vs* 10.4 cm^{-1}). The ABS white absorption coefficient however was a factor of ~ 13 lower than *in vivo* mucosal tissue (0.01 cm^{-1} for ABS white *vs* 0.13 cm^{-1} for porcine tissue). This will result in a higher fluence rate build-up factor in the ABS optical phantom as compared to the porcine tissue phantom or in a clinical setting. The average β (r) slope *a* of the ABS optical phantom was 5.2 compared to the slope of 1.3 for the porcine tissue model. This would imply that for even higher absorption, that is, increasing blood content, the slope of the β (r) approximates 1. The scatter contribution would consequently become independent of the distance between the light source and the inner tissue surface and could therefore be considered constant.

The values of the build-up factors β at the surface of the porcine tissue range between 3 and 4 for source to isotropic detector distances between ~1.5 and 2.5 cm. The β values for Barrett's esophagus ranged between 1.2 and 4 at a distance of 12.5 mm, and comparable results were demonstrated in the nasopharynx, that is, 1 and 4.4 (10,20,30). Hemoglobin is the dominant absorption chromophore in tissue at a wavelength of 652 nm. The build-up factor for *ex vivo* porcine is expected to be higher as a result of a low hemoglobin content.

The accuracy for both models was higher for the porcine phantom as compared to the ABS optical phantoms. Although the optical properties of porcine tissue are less homogeneously distributed, the shape of the geometry was less irregular (surface to volume ratio of 1.63) as compared to the ABS phantoms, this may contribute in a higher accuracy.

Zhu et al. developed an intracavity model to simulate and measure the fluence rate distribution at the pleural surface during cavity PDT of malignant mesothelioma (28,32). They incorporated a time-dependent correction factor and a constant scatter contribution that is independent of the shape of the lung cavity, to match the detector readings into their model. The pleural cavity is ellipsoidal in shape and illuminated directly after surgery. The tissue surface will therefore be dark reddish in color. If the proposed empirical model would be employed, the value for slope *a* would be low and the scatter contribution could accordingly considered to be constant. In addition, the light source is positioned centrally in the pleural cavity, which means that in these well-defined geometries the differences in distances between the light source and the detectors are relatively similar. The proposed models should generate reliable fluence rate distribution maps in case of PDT of the pleural cavity provided that the correct β (r) or *Rd* is employed.

Foscan®–mediated PDT of sinonasal malignancies is performed with a time interval of at least six weeks after surgery. This time interval was incorporated to allow the tissue to heal (*i.e.* the tissue vascular perfusion) and to have as little extravascular blood as possible in the cavity during the illumination. Besides, to minimize a surgical stress response resulting in increased cytokine release which might negatively influence the PDT effect (22). Extravascular blood shields the therapeutic light

from entering the tissue and is therefore expected to compromise the PDT effect. Note that for pleural malignant mesothelioma PDT, a six-week interval between surgery and PDT is clinically not feasible.

The sinonasal cavity is arbitrary in shape and size, which results in relatively large distances between the light source and isotropic detectors, and is expected to have a higher build-up factor due to the healed tissue. A β (r) build-up function should, for this particular PDT application, be incorporated.

As seen in Fig. 4, the experimental fluence rate data are fit with a simple linear function and intersect through coordinate (0,1). The assumption of an intersection at $r = 0$, $\beta = 1$ may not be fully accurate. If the spherical bulb diffuser is positioned close to the tissue, there will always be the local fluence rate re-emittance term (ϕ_{bsc}), which in turn depends on *Rd*. *Rd + 1*, is expected to range from 1 to < 2. This intersection uncertainty will be investigated in future studies. In addition, the exact β (r) function is more likely to be $a \cdot r^2 + b$. To confirm this assumption, an analytical derivation for β (r) and additional experimental fluence rate data for close source/surface distances are necessary.

When moving the light source closer to the tissue surface, the scatter contribution ϕ_{sc} and E_{inc} are expected to increase with $1/r^2$, resulting in a decrease in the build-up factor value at close source-surface distances. If the source is positioned in the vicinity of the center of the cavity, the scatter contribution to the surface will decrease less compared to the direct incident term E_{inc}, resulting in an increase in the build-up factor. In addition, small off-center source positions will be of limited influence on β (r). When the *Rd* of the tissue decreases, for example, in case of higher blood absorption, the slope a of the build-up factor function will decrease, and thus the scatter contribution to the total fluence rate at the tissue surface will become less.

The predictive power of the empirical model clearly depends on the number of fluence rate measurements used to determine the β function. One measurement at given known distance at a random location and one intersection point will result in a larger uncertainty in slope a resulting in a less reliable predictive power. Multiple fluence rate measurements at random locations (at different distances) however will result in a more reliable prediction. In a clinical setting, it would be feasible to measure this prior to PDT in order to predict the fluence rate in the total treatment geometry. A dedicated applicator to measure the fluence rate at least at two different fixed distances is currently under development. An example of such an applicator was demonstrated by Murrer et al. (45).

The analytical model

The model employs radiometric equations together with diffuse Lambertian re-emitting surfaces and does not take (multiple) specular reflections in consideration as expected in a mucosal tissue cavity. The main drawback of the analytic model, if considered as a clinically potential fluence rate prediction model, is that the actual patient-specific global *Rd* value is unknown. Determining the *Rd* of the three ABS optical phantoms and the porcine tissue phantom was achieved by fitting the simulation data to the measured data to achieve a minimal rms, by either increasing or decreasing *Rd* in steps of 0.01. The fit values for the *Rd* yielded 0.81 for ABS white, and for porcine tissue 0.58, respectively. The theoretical values of *Rd* according to Eq. (2) using μ_s' and μ_a of the DRS measurements and n_{rel} from literature resulted in an $Rd_{ABS} = 0.81$ and $Rd_{por} = 0.62$, respectively, and are in close agreement with those resulting from the fluence rate fit result.

Beck et al. measured a total diffuse reflectance *Rd* of *in vivo* bladder tissue of 0.59 (46). The DRS measurements on oral buccal mucosal tissue resulted in $Rd_{mucosal}$ of 0.62. The results clearly demonstrate the reliability of the analytical model. If the analytical model would be employed in a clinical setting, a series (on the various tissue types present in the sinonasal cavity) of diffuse reflectance measurements would be required in order to determine a global value for Rd_{tissue}.

The analytical model calculates a 3D fluence rate distribution map in ~16 s for a single source location (see Table 3). To find the OSL, all possible source locations within the sinonasal cavity are required for calculation. The future goal is to use an electromagnetic navigation device with a one-millimeter spatial accuracy to guide the light source to the OSL. This implies that, in case of a sinonasal cavity, an estimation of ~10,000 possible source locations need to be calculated in order to find the OSL for a single source. An efficient and fast cost function in combination with GPU computing is therefore necessary and currently being investigated. The planning is carried out prior to the PDT and therefore requires no extra time during the actual PDT treatment.

In conclusion, the predictive value of the empirical and analytical model is ~20% accurate for both types of phantoms used and was even less than 10% for the porcine tissue phantom. The presented models may generate less accurate fluence rate data in an optically inhomogeneous environment as endoscopically observed *in vivo* during sinonasal PDT. However, it still provides valuable estimated information on how the light will be distributed within the sinonasal cavity in 3D in these complex geometries, and where necrosis is likely to be expected for a given source location and output power. Table 3 suggests that repositioning the source during PDT could be employed for an improved illumination of the target area as compared to a single source position. An algorithm, for example, differential evolution, that determines one or multiple OSL's with varying output power, in order to achieve the most effective illumination at the target area, while limiting the dose delivered to the organs at risk is therefore currently under construction. This algorithm will generate the coordinates for the optimal source position that will be transferred to an electromagnetic (EM) navigation system, which helps the surgeon to guide the spherical bulb diffuser to the OSL. Baran et al. investigated intracavity PDT of deep-seated drained abscesses with complex geometries (47). The light distribution was calculated by means of Monte Carlo (MC) simulations. The delivery was performed with a bare cleaved fiber placed in the center of the volume. Their goal was to determine the optical power at which a fluence rate of 4 or 20 mW$\cdot$ cm^{-2} was achieved at 95% of the abscess wall. They showed that abscesses with a smaller surface are more amenable compared to abscesses with a larger surface. In case of sinonasal PDT, only the cavities region with residual or recurrent tumor require an effective fluence of 18–22 mW$\cdot$ cm^{-2}. Potential adjacent organs like the brain, optical nerves and carotid arteries should not exceed a fluence over 5 mW$\cdot$ cm^{-2}. Additional research will be conducted regarding: (1) the determination of *Rd* from postoperative *in vivo* sinonasal tissue μ_s' and μ_a measurements by means of multidiameter single fiber reflectance spectroscopy (MDSFR), (2) the effect of the surface to volume ratio and optical properties

on the β (r) function, (3) the incorporation of a microlens and linear diffuser source into the model and (4) the development of applicators that allow for multiple fluence rate measurements at known source-detector distances.

Acknowledgements—The research was partly funded by the Verwelius foundation (Huizen, the Netherlands) and Biolitec® (Jena, Germany). In addition, the authors like to thank Susan Brouwer de Koning for conducting the DRS measurements and Ton Vlasveld of the medical physics department for the postprocessing of the ABS optical phantoms. The Department of Head and Neck Oncology and Surgery of the Netherlands Cancer Institute receives a research grant from Atos Medical (Malmö, Sweden), which contributes to the existing infrastructure for clinical research.

REFERENCES

1. Mackenzie, G. D., N. F. Jamieson, M. R. Novelli, C. A. Mosse, B. R. Clark, S. M. Thorpe, S. G. Bown and L. B. Lovat (2008) How light dosimetry influences the efficacy of photodynamic therapy with 5-aminolaevulinic acid for ablation of high-grade dysplasia in Barrett's esophagus. *Laser Med. Sci.* **23**(2), 203–210.
2. Henderson, B. W., T. M. Busch and J. W. Snyder (2006) Fluence rate as a modulator of PDT mechanisms. *Lasers Surg. Med.* **38**(5), 489–493.
3. Tan, I. B., H. Oppelaar, M. C. Ruevekamp, R. B. Veenhuizen, A. Timmers and F. A. Stewart (1999) The importance of in situ light dosimetry for photodynamic therapy of oral cavity tumors. *Head Neck.* **21**(5), 434–441.
4. Busch, T. M., E. P. Wileyto, M. J. Emanuele, F. Del Piero, L. Marconato, E. Glatstein et al (2002) Photodynamic therapy creates fluence rate-dependent gradients in the intratumoral spatial distribution of oxygen. *Cancer Res.* **62**(24), 7273–7279.
5. Ahn, P. H., H. Quon, B. W. O'Malley, G. Weinstein, A. Chalian, K. Malloy, J. H. Atkins, T. Sollecito, M. Greenberg, S. McNulty, A. Lin, T. C. Zhu, J. C. Finlay, K. Cengel, V. Livolsi, M. Feldman, R. Mick and T. M. Busch (2016) Toxicities and early outcomes in a phase 1 trial of photodynamic therapy for premalignant and early stage head and neck tumors. *Oral Oncol.* **55**, 37–42.
6. Foster, T. H., R. S. Murant, R. G. Bryant, R. S. Knox, S. L. Gibson and R. Hilf (1991) Oxygen consumption and diffusion effects in photodynamic therapy. *Radiat. Res.* **126**(3), 296–303.
7. Cramers, P., M. Ruevekamp, H. Oppelaar, O. Dalesio, P. Baas and F. A. Stewart (2003) Foscan uptake and tissue distribution in relation to photodynamic efficacy. *Br. J. Cancer.* **88**(2), 283–290.
8. Stewart, F. A., Y. Oussoren, J. A. M. T. Poele, S. Horenblas and W. J. Mooi (1992) Functional and histological damage in the mouse bladder after photodynamic therapy. *Br. J. Cancer.* **65**(6), 884–890.
9. Shafirstein, G., D. A. Bellnier, E. Oakley, S. Hamilton, M. Habitzruther, L. Tworek, A. Hutson, J. A. Spernyak, S. Sexton, L. Curtin, S. G. Turowski, H. Arshad and B. Henderson (2018) Irradiance controls photodynamic efficacy and tissue heating in experimental tumours: implication for interstitial PDT of locally advanced cancer. *Br. J. Cancer.* **119**(10), 1191–1199.
10. van Veen, R. L., M. C. Aalders, K. L. Pasma, P. D. Siersema, J. Haringsma, W. van de Vrie, E. E. E. Gabeler, D. J. Robinson and H. J. C. M. Sterenborg (2002) In situ light dosimetry during photodynamic therapy of Barrett's esophagus with 5-aminolevulinic acid. *Lasers Surg. Med.* **31**(5), 299–304.
11. D'Cruz, A. K., M. H. Robinson and M. A. Biel (2004) mTHPC-mediated photodynamic therapy in patients with advanced, incurable head and neck cancer: a multicenter study of 128 patients. *Head Neck.* **26**(3), 232–240.
12. Civantos, F. J., B. Karakullukcu, M. Biel, C. E. Silver, A. Rinaldo, N. F. Saba, R. P. Takes, V. Vander Poorten and A. Ferlito (2018) A review of photodynamic therapy for neoplasms of the head and neck. *Adv. Ther.* **35**(3), 324–340.
13. Karakullukcu, B., K. van Oudenaarde, M. P. Copper, W. M. Klop, R. van Veen, M. Wildeman and I. Bing Tan (2011) Photodynamic therapy of early stage oral cavity and oropharynx neoplasms: an outcome analysis of 170 patients. *Eur. Arch. Otorhinolaryngol.* **268**(2), 281–288.
14. Meulemans, J., P. Delaere and Poorten V. Vander (2019) Photodynamic therapy in head and neck cancer: indications, outcomes, and future prospects. *Curr. Opin. Otolaryngol. Head Neck Surg.* **27**(2), 136–141.
15. Jerjes, W., T. Upile, Z. Hamdoon, C. A. Mosse, S. Akram and C. Hopper (2011) Photodynamic therapy outcome for oral dysplasia. *Lasers Surg. Med.* **43**(3), 192–199.
16. Mimikos, C., G. Shafirstein and H. Arshad (2016) Current state and future of photodynamic therapy for the treatment of head and neck squamous cell carcinoma. *World J. Otorhinolaryngol. Head Neck Surg.* **2**(2), 126–129.
17. Quon, H., C. E. Grossman, J. C. Finlay, T. C. Zhu, C. S. Clemmens, K. M. Malloy and T. M. Busch (2011) Photodynamic therapy in the management of pre-malignant head and neck mucosal dysplasia and microinvasive carcinoma. *Photodiagnosis Photodyn. Ther.* **8**(2), 75–85.
18. van Straten, D., V. Mashayekhi, H. S. de Bruijn, S. Oliveira and D. J. Robinson (2017) Oncologic photodynamic therapy: basic principles, current clinical status and future directions. *Cancers (Basel).* **9**(12), 19.
19. Grossman, C., T. Zhu, J. Finlay, A. Dimofte, K. Malloy, B. Jr O'Malley, G. Weinstein, T. M. Busch and H. Quon (2010) Targeted laryngeal photodynamic therapy with a balloon diffusing light source. *Photodiagnosis Photodyn. Ther.* **7**(3), 158–161.
20. Nyst, H. J., R. L. van Veen, I. B. Tan, R. Peters, S. Spaniol, D. J. Robinson, F. A. Stewart, P. C. Levendag and H. J. C. M. Sterenborg (2007) Performance of a dedicated light delivery and dosimetry device for photodynamic therapy of nasopharyngeal carcinoma: phantom and volunteer experiments. *Lasers Surg. Med.* **39**(8), 647–653.
21. Caesar, L., T. E. van Doeveren, I. B. Tan, A. Dilci, R. L. van Veen and B. Karakullukcu (2015) The use of photodynamic therapy as adjuvant therapy to surgery in recurrent malignant tumors of the paranasal sinuses. *Photodiagnosis Photodyn. Ther.* **12**(3), 414–421.
22. van Doeveren, T. E. M., M. B. Karakullukcu, R. L. P. van Veen, M. Lopez-Yurda, W. H. Schreuder and I. B. Tan (2018) Adjuvant photodynamic therapy in head and neck cancer after tumor-positive resection margins. *Laryngoscope.* **128**(3), 657–663.
23. Star, W. M. (1990) Light delivery and light dosimetry for photodynamic therapy. *Laser Med. Sci.* **5**(107), 107–113.
24. van Staveren, H. J., R. H. Bertrams and W. M. Star (1997) Bladder PDT with intravesical clear and light scattering media: effect of an eccentric isotropic light source on the light distribution. *Lasers Surg. Med.* **20**(3), 248–253.
25. Marijnissen, J. P. A. and W. M. Star (1987) Quantitative light dosimetry in vitro and in vivo. *Laser Med. Sci.* **2**(235), 235–42.
26. Star, W. M. (1995) The relationship between integrating sphere and diffusion theory calculations of fluence rate at the wall of a spherical cavity. *Phys. Med. Biol.* **40**(1), 1–8.
27. Dimofte, A., T. C. Zhu, J. C. Finlay, M. Cullighan, C. E. Edmonds, J. S. Friedberg, Cengel, K. and S. M. Hahn (2009) In-vivo light dosimetry for pleural PDT. *Proc. SPIE Int. Soc. Opt. Eng*. **7164**
28. Zhu, T. C., M. M. Kim, J. Padawer, A. Dimofte, M. Potasek, K. Beeson and E. Parilov (2018) Light fluence dosimetry in lung-simulating cavities. *Proc. SPIE Int. Soc. Opt. Eng*. **10476**
29. Murrer, L. H., K. M. Hebeda, J. P. Marijnissen and W. M. Star (1999) Short- and long-term normal tissue damage with photodynamic therapy in pig trachea: a fluence-response pilot study comparing photofrin and mTHPC. *Br. J. Cancer.* **80**(5–6), 744–755.
30. van Veen, R. L., H. Nyst, S. Rai Indrasari, M. Adham Yudharto, D. J. Robinson, I. B. Tan, Meewis, C., R. Peters, S. Spaniol, F. A. Stewart, P. C. Levendag and H. J. Sterenborg (2006) In vivo fluence rate measurements during Foscan-mediated photodynamic therapy of persistent and recurrent nasopharyngeal carcinomas using a dedicated light applicator. *J. Biomed. Opt.* **11**(4), 041107.
31. Beyer, W. (1996) Systems for light application and dosimetry in photodynamic therapy. *J. Photochem. Photobiol. B.* **36**(2), 153–156.
32. Betrouni, N., C. Munck, W. Bensoltana, G. Baert, A. S. Dewalle-Vignion, A. Scherpereel and S. Mordon (2017) Real-time light dosimetry for intra-cavity photodynamic therapy: application for pleural mesothelioma treatment. *Photodiagnosis Photodyn. Ther.* **18**, 155–161.

33. Dimofte, A., J. C. Finlay, A. V. Sharikova, K. A. Cengel, P. Ahn, T. M. Busch, Ahn, P., T. M. Busch and T. C. Zhu (2014) Determination of tissue optical properties in PDT treated head & neck patients. *Proc. SPIE Int. Soc. Opt. Eng*. **8926**.
34. Ong, Y. H., J. Padawer-Curry, J. C. Finlay, M. M. Kim, A. Dimofte, K. Cengel and Zhu, T. C. (2018) Determination of optical properties, drug concentration, and tissue oxygenation in human pleural tissue before and after Photofrin-mediated photodynamic therapy. *Proc. SPIE Int. Soc. Opt Eng*. **10476**
35. Karakullukcu, B., S. C. Kanick, J. B. Aans, H. J. Sterenborg, I. B. Tan, A. Amelink et al (2011) Clinical feasibility of monitoring m-THPC mediated photodynamic therapy by means of fluorescence differential path-length spectroscopy. *J. Biophotonics.* **4**(10), 740–751.
36. Middelburg, T. A., C. L. Hoy, H. A. Neumann, A. Amelink and D. J. Robinson (2015) Correction for tissue optical properties enables quantitative skin fluorescence measurements using multi-diameter single fiber reflectance spectroscopy. *J Dermatol. Sci.* **79**(1), 64–73.
37. Sandell, J. L. and T. C. Zhu (2011) A review of in-vivo optical properties of human tissues and its impact on PDT. *J Biophotonics.* **4**(11–12), 773–787.
38. Diep, P., S. Pannem, J. Sweer, J. Lo, M. Snyder, G. Stueber, Y. Zhao, S. Tabassum, R. Istfan, J. Wu, S. Erramilli and D. Roblyer (2015) Three-dimensional printed optical phantoms with customized absorption and scattering properties. *Biomed. Opt. Express.* **6**(11), 4212–4220.
39. van der Heijden, F. (1994) *Image Based Measurement Systems: Object Recognition and Parameter Estimation*, p. 338p. Wiley, Chichester.
40. Brouwer de Koning, S. G., E. J. M. Baltussen, M. B. Karakullukcu, B. Dashtbozorg, L. A. Smit, R. Dirven, B. H. W. Hendriks, H. J. C. M. Sterenborg and T. J. M. Ruers (2018) Toward complete oral cavity cancer resection using a handheld diffuse reflectance spectroscopy probe. *J. Biomed. Opt.* **23**(12), 1–8.
41. Fedorov, A., R. Beichel, J. Kalpathy-Cramer, J. Finet, J. C. Fillion-Robin, S. Pujol, C. Bauer, D. Jennings, F. Fennessy, M. Sonka, J. Buatti, S. Aylward, J. V. Miller, S. Pieper and R. Kikinis (2012) 3D Slicer as an image computing platform for the Quantitative Imaging Network. *Magn. Reson. Imaging.* **30**(9), 1323–1341.
42. Farrell, T. J., M. S. Patterson and B. Wilson (1992) A diffusion theory model of spatially resolved, steady-state diffuse reflectance for the noninvasive determination of tissue optical properties in vivo. *Med. Phys.* **19**(4), 879–888.
43. Dimofte, A., T. C. Zhu, S. M. Hahn and R. A. Lustig (2002) In vivo light dosimetry for motexafin lutetium-mediated PDT of recurrent breast cancer. *Lasers Surg. Med.* **31**(5), 305–312.
44. van Veen, R. L., H. J. Sterenborg, A. W. Marinelli and M. Menke-Pluymers (2004) Intraoperatively assessed optical properties of malignant and healthy breast tissue used to determine the optimum wavelength of contrast for optical mammography. *J. Biomed. Opt.* **9**(6), 1129–1136.
45. Murrer, L. H., J. P. Marijnissen, P. Baas, N. Van Zandwijk and W. M. Star (1997) Applicator for light delivery and in situ light dosimetry during endobronchial photodynamic therapy: first measurements in humans. *Lasers Med. Sci.* **12**(3), 253–259.
46. Beck, T. J., W. Beyer, T. Pongratz, W. Stummer, R. Waidelich, H. Stepp, Wagner, S. and Baumgartner, R. (2003) Clinical determination of tissue optical properties in vivo by spatially resolved reflectance measurements. *P. Soc. Photo-Opt. Ins.* **5138**, 96–105.
47. Baran, T. M., H. W. Choi, M. J. Flakus and A. K. Sharma (2019) Photodynamic therapy of deep tissue abscess cavities: retrospective image-based feasibility study using Monte Carlo simulation. *Med. Phys.* **46**(7), 3259–3267.